Particle trajectories, gamma-ray emission, and anomalous radiative trapping effects in magnetic dipole wave

A. V. Bashinov [1,*] E. S. Efimenko [1] A. A. Muraviev [1] V. D. Volokitin,[2] I. B. Meyerov,[2]
G. Leuchs,[1,3] A. M. Sergeev,[1] and A. V. Kim[1]

[1]*Institute of Applied Physics, Russian Academy of Sciences, Nizhny Novgorod 603950, Russia*
[2]*Lobachevsky State University of Nizhny Novgorod, Nizhny Novgorod 603950, Russia*
[3]*Max Planck Institute for the Science of Light, Erlangen, Germany*

In studies of interaction of matter with laser fields of extreme intensity there are two limiting cases of a multibeam setup maximizing either the electric field or the magnetic field. In this work attention is paid to the optimal configuration of laser beams in the form of an m-dipole wave, which maximizes the magnetic field. We consider in such highly inhomogeneous fields the advantages and specific features of laser-matter interaction, which stem from individual particle trajectories that are strongly affected by gamma photon emission. It is shown that in this field mode qualitatively different scenarios of particle dynamics take place in comparison with the mode that maximizes the electric field. A detailed map of possible regimes of particle motion (*ponderomotive trapping*, *normal radiative trapping*, *radial*, and *axial anomalous radiative trapping*), as well as angular and energy distributions of particles and gamma photons, is obtained in a wide range of laser powers up to 300 PW, and it reveals signatures of radiation losses experimentally detectable even with subpetawatt lasers.

I. INTRODUCTION

Currently, actively developing multipetawatt laser facilities [1] have the potential to become a unique tool for studying the properties of quantum vacuum and quantum electrodynamics (QED) processes in extremely strong fields [2,3], as well as for modeling astrophysical phenomena in laboratory conditions [4–6]. Previously, the main attention has been paid to optimal configurations of the multibeam laser setup in which the electric field attains the maximal value. In this case the electric field assumes the leading role in establishing the main physical effects, for example, direct tunneling ionization of vacuum by laser pulses [7–11]. For such field structures detailed studies have also been done with respect to gamma-ray emission, QED cascades and electron-positron pair plasma production (see also [12–22]). Particularly, in the limiting case of the converging e-dipole wave [23], characterized by a minimal focal volume and the maximal electric field for a given power, extreme plasma states can be created, paving the way to quantum pair plasma and the Schwinger field [24,25]. However, there are also many fundamental effects in which the magnetic field is a key factor, for example, high energy electrons radiate gamma photons mainly on the curved part of their trajectories induced by a strong magnetic field [26]. Consequently, the choice of field structure in a laser multibeam configuration should depend on the specific physical effects of interest in extreme laser-matter interactions.

In this paper we pay attention to the case of tightly focused laser beams that maximize the magnetic field, and

begin our consideration with the limiting case corresponding to a converging m-dipole wave. We keep in mind such an important problem as vacuum breakdown in tightly focused laser beams and dense pair plasma production in the laboratory [9,14,16,19,24,25,27–31]. In this problem both electric and magnetic fields are equally important. An electron is accelerated to high energy in the driving electric field, but photons are emitted mainly on a curved trajectory in the strong magnetic field [32,33]. Photon decay into an electron-positron pair also occurs mainly in the strong magnetic field [32]. In turn, after being born electrons and positrons may get accelerated to high energies by the electric field. Thus, both electric and magnetic domains in space and time contribute significantly [32] to the pair avalanche [12] in tightly focused beams. Our aim is to show advantages and specific features of the laser-matter interaction at extreme intensities in highly inhomogeneous fields of the m-dipole wave, identify the experimental signatures for detecting these features, as well as investigate new pair plasma states that can be produced in the laboratory. The problem is complex and, since laser-matter interaction in these fields has not yet been investigated, certain studies should be completed from the ground up, starting from single-particle trajectories and gamma photon emission, following with vacuum breakdown and the nonlinear stage of laser plasma interactions. This paper is devoted to studying particle trajectories[1] in such highly inhomogeneous fields in a wide range of powers from 0.01 to 300 PW. Trajectories not only shape the evolution of the particle ensemble but

---

*bashinov@ipfran.ru

[1]Within this work the term particle refers only to electrons and positrons.

also define QED processes: particles emit gamma photons which in turn can decay into electron-positron pairs in laser fields [34].

This paper is organized as follows. In Sec. II A we briefly discuss the standing wave approach in the analysis of particle motion and pair plasma generation. In Sec. II B we demonstrate the distributions of electric and magnetic fields of the m-dipole wave. In Sec. III A we present general properties of particle motion and in Sec. III B we describe the employed numerical setup. In Secs. III C and III D based on the time evolution of the particle ensemble, its spatial distribution, energy, and angular spectra we propose several characteristics in order to reveal distinctions in particle motion caused by radiation losses and determine threshold powers of possible modes of motion. In Sec. III E we analyze in more detail particle trajectories within the determined characteristic power ranges. In Sec. III F properties of the gamma emission generated on these trajectories are considered. In Sec. IV, based on specific features of energy and angular distributions of particles and photons, an experimental approach for detection of signatures of radiation losses is proposed. Finally, in Sec. V the results are summarized.

II. FORMULATION OF THE PROBLEM

A. General approach

In order to generate pair plasma by incoming laser pulses we must prepare a seed to trigger vacuum breakdown. A seed can be an electron beam, a gas or solid target, or a gamma ray (for example, see [35–39]). First of all, the interaction of a seed with the leading edge of laser pulses must ensure that a number of seed particles reach the region of sufficiently strong fields and that fields are not strongly screened [40] by seed particles swept to this region. The next important question is how seed particles move in the strong field region, because this determines basic processes of vacuum breakdown such as photon (pair) production and particle escape from this region.

An advantageous field configuration for vacuum breakdown is colliding laser beams [12,16,22]. The strongest fields achieved in the beams' focal region are favorable for abundant emission of gamma photons and their decay. Moreover, such fields can enable radiative trapping [33,41,42], which de-

creases the rate of escape of electrons (positrons) from focus. Most of the time in the focal region particle motion is influenced by a superposition of colliding pulses. Since in order to trigger vacuum breakdown fields of incident pulses should not be strongly screened, vacuum breakdown can be studied in given fields, i.e., fields generated by seed particles can be neglected. Even within this assumption, resulting fields can have quite a complex space-time structure depending on depth of focus, pulse envelopes, etc. All these factors complicates analysis of basic processes of vacuum breakdown. However, in the case of tight focusing the focal region has a subwavelength spatial scale (about half of wavelength) where particle motion and emission of gamma photons as well as their decay become particularly important. In this region the resulting fields can be approximated with high accuracy by fields of a standing wave. We use this assumption in order to pave the way to studying vacuum breakdown in the colliding laser beams focused in the form of the m-dipole wave. Below we will consider electron (positron) motion in the given fields of the standing m-dipole wave depending on the wave power and show that the obtained results allow revealing a quantum signature of photon recoil when a converging pulsed m-dipole wave irradiates a solid target.

B. Field structure of the m-dipole wave

For clarity we briefly introduce the field structure of the standing m-dipole wave and describe its features. Its magnetic field has a poloidal structure and the electric field is toroidal. The field structure possesses axial symmetry. We define a point on the axis of symmetry, where the magnetic field amplitude is maximal, as the central point and let it coincide with the coordinate origin. Without loss of generality we assume that the axis of symmetry is the z axis, then the main component of the magnetic field in the vicinity of the central point is the z component. Both electric and magnetic fields are strongest at the central plane passing through the central point perpendicular to the z axis. Outside the central plane due to the poloidal structure the magnetic field also has a radial component in the cylindrical coordinate system. The electric field is purely azimuthal.

The exact analytical expressions for fields of the standing m-dipole wave are the following [23]:

$$\mathbf{E} = F_0 \sqrt{P_{\mathrm{PW}}} \cos(\omega t) \frac{\rho}{R} \left[\frac{\sin(kR)}{(kR)^2} - \frac{\cos(kR)}{kR} \right] \mathbf{e}_\varphi,$$

$$\mathbf{B} = -F_0 \sqrt{P_{\mathrm{PW}}} \sin(\omega t) \left\{ \left[\frac{\sin(kR)}{kR} \left(1 - \frac{1+(kz)^2}{(kR)^2} + \frac{3(kz)^2}{(kR)^4} \right) + \frac{\cos(kR)}{(kR)^2} \left(1 - \frac{3(kz)^2}{(kR)^4} \right) \right] \mathbf{e_z} \right.$$

$$\left. + \frac{\rho z}{R^2} \left[\frac{\sin(kR)}{kR} \left(\frac{3}{(kR)^2} - 1 \right) - \frac{3\cos(kR)}{(kR)^2} \right] \mathbf{e_\rho} \right\}, \tag{1}$$

where P is the wave power, $P_{\mathrm{PW}} = P/(1\ \mathrm{PW})$ is the dimensionless wave power, $F_0 = \frac{2e}{mc^2}\sqrt{\frac{3}{c}}10^{22}\ \mathrm{erg\ s^{-1}} \approx 1174$, $e = 4.8\times10^{-10}$ statC is the elementary charge, m is the positron mass, c is the light velocity, t is time, $\omega = 2.1\times10^{15}\ \mathrm{s^{-1}}$ is the

wave frequency corresponding to the wave period $T = 3$ fs and the wavelength $\lambda = 0.9\ \mu\mathrm{m}$, $k = \omega/c$ is the wave number, ρ and z are radial and axial coordinates in the cylindrical coordinate system, $R = \sqrt{\rho^2 + z^2}$, and $\mathbf{e}_{\rho,\varphi,z}$ are unit vectors.
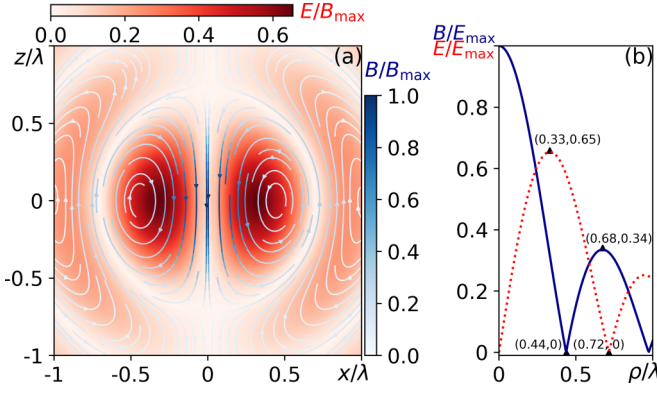
FIG. 1. Spatial distribution of electric and magnetic fields of the standing m-dipole wave. The electric field distribution and magnetic field lines are presented in panel (a) in coordinates z and x in the Cartesian coordinate system. Electric (dotted line) and magnetic (solid line) fields as function of ρ in the central plane are shown in panel (b). Triangle markers denote locations and values of field extrema.

Fields are normalized to the relativistic value $mc\omega/e$. Distributions of electric and magnetic fields are shown in Fig. 1.

The characteristic field extrema are shown in Fig. 1(b). The maximum amplitude of the magnetic field $a_B = a$ is achieved at the central point $\rho = 0$, $z = 0$ and the maximum amplitude of the electric field a_E is achieved on a circle in the central plane $z = 0$ with radius $\rho_m = 0.33\lambda$. The dependencies of field amplitudes on the dimensionless power P_{PW} are as follows:

$$a_B = a = 2F_0\sqrt{P_{PW}}/3 \approx 780\sqrt{P_{PW}},$$
$$a_E = 0.65a \approx 510\sqrt{P_{PW}}. \tag{2}$$

The first node of the electric field coincides with the z axis, and the second electric field node lies approximately on the sphere with the radius of 0.72λ. Near the central point electric and magnetic fields can be approximated as

$$\mathbf{E} \approx ak\rho\left(\frac{1}{2} - \frac{(kz)^2}{20}\right)\mathbf{e}_\varphi,$$

$$\mathbf{B} \approx a\left\{\left[\left(1 - \frac{(kz)^2}{10}\right) + (k\rho)^2\left(\frac{(kz)^2}{70} - \frac{1}{5}\right)\right]\mathbf{e}_z + \frac{k^2z\rho}{10}\mathbf{e}_\rho\right\}. \tag{3}$$

III. MODES OF PARTICLE MOTION

A. General view

One of the main objectives of this work is to classify possible regimes of particle motion depending on the power of incident waves, and to select the most characteristic ones which can either determine the dynamics of vacuum breakdown or possess new fundamental properties, including those useful for possible applications. In the fields of tightly focused waves the motion of particles is in general three-dimensional, and it strongly depends on the initial conditions: particle position, its momentum, initial phase of fields. Such a multidimensional problem is challenging not only for analytical consideration but even for numerical simulations. To get

started, we look at the general properties which can be studied analytically.

First, the motion in fields of an m-dipole wave is essentially three-dimensional. We stress it here, because in the case of an e-dipole wave, particle trajectories mainly lie in the plane (z, ρ), since the magnetic field is purely azimuthal and there is no force acting on the particle in the azimuthal direction[2] [33,43]. In contrast, in fields of an m-dipole wave the deflection from planar motion occurs because the electric field drives the particle in the azimuthal direction, while the magnetic part of the Lorentz force excites radial and axial motion.

Second, particles oscillating along the azimuth experience centrifugal force. This force is represented by the second term in the radial projection of the motion equation in the cylindrical coordinate system, while the first term $F_{L\rho}$ is the radial projection of the Lorentz force:

$$\frac{dp_\rho}{dt} = F_{L\rho} + \frac{p_\varphi^2}{m\gamma\rho}, \tag{4}$$

where p_ρ and p_φ are the radial and azimuthal components of particle momentum, m and γ are the particle mass and the Lorentz factor. Note that for particles at rest the centrifugal force arises due to the azimuthal electric field. The last term in Eq. (4) is absent in fields of the e-dipole wave, where motion is radial and axial.

Third, when the radiation losses can be neglected, then the system of equations of motion is a Hamiltonian system and the axial component of the canonical angular momentum M_z is a constant of motion due to the axial field symmetry:

$$M_z = \rho(p_\varphi + q_p A_\varphi/c) = \text{const}, \tag{5}$$

where A_φ is the azimuthal component of the vector-potential and q_p is the particle charge. If initially a particle is at rest and $A_\varphi(t = 0) = 0$ in accordance with Eq. (1) (or in the case of an incident laser pulse colliding with a particle at rest) the constant of motion corresponds to the zero canonical momentum, therefore

$$p_\varphi = -q_p A_\varphi/c. \tag{6}$$

If we take into account radiation losses as a sequence of acts of photon emission then between these acts $M_z = \text{const}$, however, after each act the constant changes.

Fourth, in the ultrarelativistic case $\gamma \gg 1$, according to the motion equations the particle momentum $\mathbf{p}$ linearly depends on field amplitude in fields of the standing wave without photon recoil, $|\mathbf{p}| \sim \gamma \sim a$. Thus, it follows from $d\mathbf{r}/dt = \mathbf{p}/(m\gamma)$ that the position vector $\mathbf{r}$ is independent on field amplitude. As a result, comparison of the particle distribution as a function of $\mathbf{p}/a$ or $\mathbf{r}$ with and without photon recoil gives evidence of radiative effects.

---

[2] In the general case this statement is absolutely correct only if there is no initial azimuthal momentum. However, in the radiation-dominated regime, which is the subject of interest, the statement is correct in a broader sense, because this momentum component quickly decays due to radiation losses and there are no forces exciting motion in the azimuthal direction.

B. Numerical setup

For modeling of particle motion we use the QED-PIC code PICADOR [44], which simulates photon emission by particles as random acts with the help of the Monte Carlo method [45] based on QED probabilities within local constant field approximation [34,46]. Between acts of photon emission particles experience only the Lorentz force. This method for the simulation of photon emission is usually called quantum or quasiclassical (the terminology may differ) and is widely used in leading studies as a benchmark; for example see Refs. [14,18,21,22,27,30,36,47–49]. Additionally, the code PICADOR has an option which allows considering radiation losses as the Landau-Lifshitz force [26,50] or excluding radiative recoil in order to simulate motion of particles which can emit photons but experience only the Lorentz force. These options are very useful to compare results of simulations with and without radiation losses within different approaches.

In order to identify regimes of particle motion and retrieve different characteristics of dynamics of the particle ensemble, in the next sections we consider the following numerical setup. Probe electrons and positrons are initially distributed uniformly within a sphere with the radius of 0.6λ and the center coinciding with the central point. The initial number of particles of each type is 3×10^6, fields are set analytically according to Eq. (1). The size of the simulation box is $6\lambda \times 6\lambda \times 6\lambda$ along x, y and z axes and the number of cells along them is $600 \times 600 \times 600$. The time step is $T/260$. The wave power varies from 0.01 to 300 PW.

C. Particle escape

First of all, we would like to point out that stochasticity of photon emission and particle escape from the focus due to strong field inhomogeneity significantly complicate the analysis of particle motion. The stationary particle distributions provide simple and rigorous criteria of different modes of motion. In the case of strongly inhomogeneous fields such distributions are not formed like they are in a plane wave [33,42,49,51,52]. However, it is reasonable to consider that specific features of particle motion in the focal region influence particle escape, whose properties allow identifying different regimes of motion [53]. Following this idea, in this section the temporal evolution of the particle ensemble in the focus is studied.

Simulations show that particles inevitably leave the focal region, so N_{sp} (the particle number within the initial sphere) decreases. At powers $P \lesssim 1$ PW this number $N_{sp}(t)$ decreases monotonically with time [see Fig. 2(a)], while at greater powers $N_{sp}(t)$ is modulated at the doubled wave frequency as shown in Figs. 2(b) and 2(c). Simulations without photon recoil confirm that these modulations result from radiation losses, because without photon recoil $N_{sp}(t)$ at $P > 1$ PW matches the one at $P \lesssim 1$ PW and all of them are monotonic.

In order to retrieve the characteristic time of change of $N_{sp}(t)$ the Savitzky-Golay filter [54] is applied. This filter smoothes modulations and allows obtaining $\overline{N}_{sp}(t)$, which is the average particle number within the initial sphere. A common characteristic time of particle escape t_e defined as $\overline{N}_{sp}(t_e) = N_{sp}(0)/e$ is shown in Fig. 2(d). On the one hand it
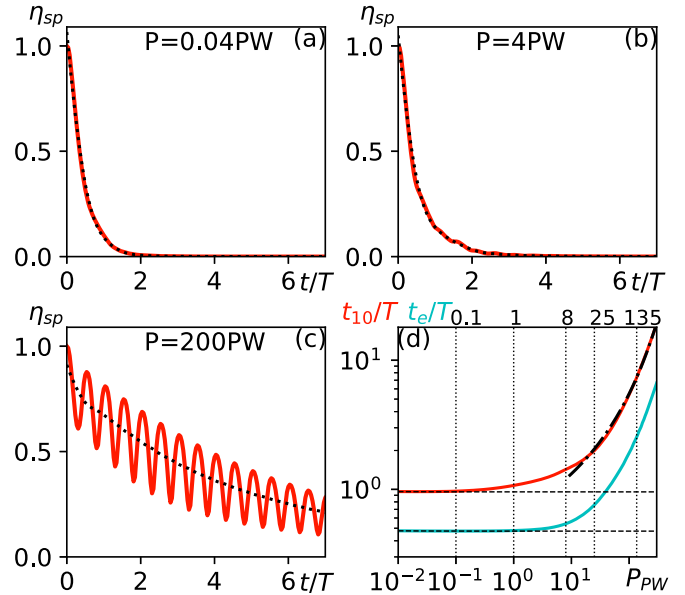

FIG. 2. Temporal evolution of particle number in a centered sphere with the radius of 0.6λ normalized to its initial value $\eta_{sp}(t) = N_{sp}(t)/N_{sp}(0)$ for different wave powers: (a) $P = 0.04$ PW; (b) $P = 4$ PW; (c) $P = 200$ PW. Red (dark gray) solid lines correspond to primary data of numerical simulations, black dotted lines are results of their smoothing by Savitzky-Golay filter. (d) Dependencies of time intervals t_{10} [red (dark gray) solid line] and t_e [pale blue (gray) solid line] on the wave power. For comparison the corresponding time intervals obtained without photon recoil are shown by black dashed lines. Dash-dotted line shows an approximation of t_{10} at powers $P > 25$ PW. Vertical dotted lines correspond to threshold powers of different regimes of motion.

characterizes radiative effects: above $P \approx 1$ PW t_e increases, which indicates this value of power as one of the thresholds. On the other hand particles may need a longer time than t_e to accumulate radiative effects and begin oscillating in a quasi-steady-state radiative regime. For this reason we introduce a more general characteristic time t_q as $\overline{N}_{sp}(t_q) = N_{sp}(0)/q$, where q is a parameter (positive real number), and the larger q the larger t_q. Simulations show that the form of $t_q(P)$ almost stops changing at $q > 7$. So, instead of t_e the time interval t_{10} is more sensitive to radiative effects which emerge even at $P \gtrsim 0.1$ PW according to t_{10} [compare red (dark gray) solid and dashed black lines in Fig. 2(d)].

Thus, analysis of the character of particle escape reveals two threshold powers $P_1 \approx 0.1$ PW and $P_2 \approx 1$ PW which indicate changes in the evolution of particle distribution. These thresholds are marked by vertical dashed lines in Fig. 2(d). However, at greater powers, when radiation losses should become more and more prominent, dependencies $t_{10}(P)$ and $t_e(P)$ do not allow distinguishing any evident thresholds. These thresholds [vertical dashed lines at $P > P_2$ in Fig. 2(d)] will be obtained in the next section.

D. Spatial distributions, energy, and angular spectra of particles

Along with the temporal evolution of the particle ensemble in the focus, its spatial distribution at particular moments of time as well as energy and angular distributions of particles

all have imprints of specific features of motion and provide an opportunity to distinguish different regimes of interaction. According to the dependence of particle motion on wave power in the ultrarelativistic case discussed in Sec. III A, the spatial distribution of particles and their distribution in momentum space with respect to **p**/a should clearly demonstrate radiative effects. In this section we determine characteristic power thresholds of different regimes of motion based on an analysis of proposed distributions.

One of the distributions is the spatial particle distribution, which directly depends on the motion of particles. Their motion in the fields of the m-dipole wave is essentially three-dimensional and a scan over the wave power adds a fourth parameter to analysis. However, the number of dimensions can be reduced due to several aspects. First, although particles oscillate along the azimuth, their motion does not depend on the azimuthal angle due to axial field symmetry. Thus, this symmetry allows eliminating the azimuthal angle from the parameter space. Second, it is reasonable to consider particles in the vicinity of the central plane, because these particles need more time to escape the focal region and, as a consequence, the influence of radiative losses on these particles is more prominent. Averaging of the particle distribution over a thin layer near the central plane allows eliminating the z coordinate from the parameter space. Third, to make the spatial distribution more stable and independent of time, we average it over a few laser periods starting from the particular moment of time $t^* = t_{10}$, when regimes of motion are steady-state. As a result, the scan of the averaged radial distribution of particles over the wave power produces a two-dimensional map $\bar{n}(\rho, P)$ [Figs. 3(a) and 3(b)], which can be used to reveal radiation-dominated regimes. A more detailed explanation of how to retrieve $\bar{n}(\rho, P)$ from simulations is given in Appendix A.

Although $\bar{n}(\rho)$ may be quite informative, it is difficult to obtain this distribution in experiments. From a practical point of view angular distributions and energy spectra of particles escaping the focal region can provide experimental evidence of regimes of motion. By analogy with $\bar{n}$, averaged angular $\overline{W}'_{\Omega}$ and energy $\overline{W}'_{\varepsilon_r}$ characteristics can be introduced. These characteristics at different wave powers are shown in Figs. 3(c)–3(f). Below we shortly describe their meanings, a more detailed explanation is given in Appendix A.

The distinctive feature of these characteristics is that they are measured at a distance from the focus: namely, at the surface of an observation sphere with radius r_{obs}, which is equal to half of the size of the simulation box. Thus, an event in the focal region can be observed via these characteristics with delay $t_d \approx r_{obs}/c$ later, in our simulations $t_d \approx 3T$.

$\overline{W}'_{\Omega}(\Omega)$ as a function of solid angle Ω in the momentum space denotes the averaged over time energy of particles crossing the observation sphere with momentum directed into an element of solid angle $d\Omega$ in the momentum space. Note that the angular distribution in the momentum space measured in the micron-sized region is relevant to the angular distribution in coordinate space at a much larger distance, where experimental detectors are usually placed. $\overline{W}'_{\Omega}(\Omega)$ is uniform along the azimuth owing to the symmetry of the field structure, so it is enough to analyze only $\overline{W}'_{\Omega}(\theta)$ as a function of
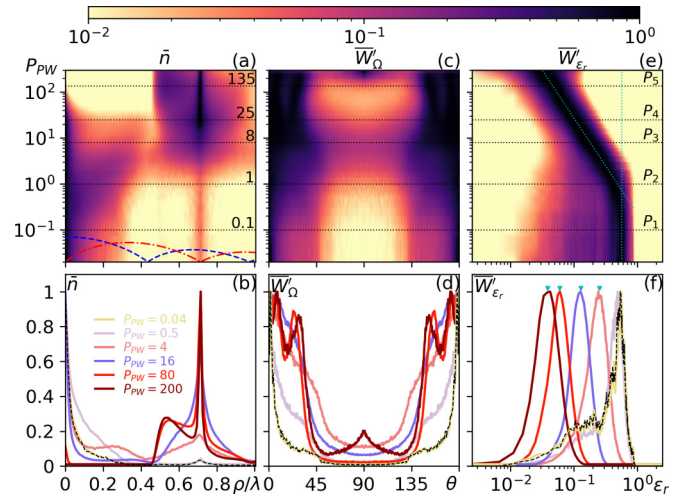

FIG. 3. (a) Radial distribution of particles $\bar{n}$ as function of wave power. Blue (black) dashed and red (gray) dash-dotted lines correspond to distributions of magnetic and electric field amplitudes along the radial direction in the central plane. Maps of angular $\overline{W}'_{\Omega}$ and energy $\overline{W}'_{\varepsilon_r}$ distributions of particles crossing the observation sphere as functions of wave power are presented in panels (c) and (e), respectively. Horizontal black dotted lines show power threshold of different dynamics of the particle ensemble. Dotted vertical and sloped cyan (gray) lines in panel (e) correspond to approximations of maxima locations $\varepsilon_{r,m}$ of $\overline{W}'_{\varepsilon_r}$: $\varepsilon_{r,m} \approx 0.6$ and $\varepsilon_{r,m} \approx 0.5 P_{PW}^{-0.48}$, respectively. Locations of maxima of $\overline{W}'_{\varepsilon_r}$ according to the last approximation are depicted by cyan (gray) arrows in panel (f). Examples of averaged distributions at different powers are depicted in panels (b), (d), and (f) by colored lines (in shades of gray). For comparison, distributions obtained without photon recoil are shown with black dashed lines.

the polar angle θ (measured from the positive direction of the z axis).

Unlike angular and spatial characteristics the energy spectrum depends on power in the case without photon recoil. However, the spectrum as a function of normalized energy

$$\varepsilon_r = \varepsilon/(mc^2 a_E) \quad (7)$$

(ε is the particle energy) maintains its form in this case at different relativistic powers and can be considered as a sensitive characteristic of radiative effects. The spectrum as function of ε_r we call *relative* spectrum. For analysis of regimes of motion we consider the averaged in time *relative* spectrum $\overline{W}'_{\varepsilon_r}(\varepsilon_r)$ of particles crossing the observation sphere as a function of the normalized particle energy.

Based on the introduced characteristics we have revealed five power thresholds ($P_1 = 0.1$ PW, $P_2 = 1$ PW, $P_3 = 8$ PW, $P_4 = 25$ PW, $P_5 = 135$ PW); see Fig. 3. Note, that first two power thresholds (P_1 and P_2) are the same as discussed in the previous section.

At powers $P < P_1 = 0.1$ PW the main regimes of motion are *ponderomotive trapping* and *ponderomotive escape*. In these regimes the proposed spatial, angular and energy characteristics are almost independent of power and they are very close to those obtained in the case without photon recoil, so it can be concluded that in this case radiative effects are

negligible. Ponderomotively trapped particles oscillate around electric field nodes. Respectively, there are two peaks of particle density: the first one is at the first electric field node (the central point) and a much weaker peak is at the second electric field node ($\rho \approx 0.72\lambda$); see Figs. 3(a) and 3(b). Note that in the considered power range almost all particles are concentrated at $\rho < \rho_m = 0.33\lambda$, and there is almost no particles between the first electric field antinode and the second electric field node. Trapped particles escape the focal region close to the z axis ($\theta \approx 0°$, $180°$) with an angular spread of about $5°$ and transverse particle escape is insignificant [see Figs. 3(c) and 3(d)]. Since radiation losses are negligible, many particles can gain a high energy $\varepsilon_{r,m} \approx 0.6$ and escape the focus without losing a large part of their energy [see Figs. 3(e) and 3(f)]. The spread of normalized energy is determined mainly by initial conditions and is relatively small. Note that most of the particles initially located at $\rho > \rho_m$ quickly escape the focal region within $t < t_{10}$ and these particles do not contribute to the averaged characteristics presented in Fig. 3. Motion of these particles can be called *ponderomotive escape* because the direction of their escape is mainly determined by field gradients.

At powers $P \geqslant P_1$ radiation losses become noticeable and a new regime of motion comes forth. It can be named *anomalous radiative trapping* (ART) [33]. We emphasize that the threshold of the ART regime corresponds to relatively low field amplitudes in relativistic units: $a_B = 250$ and $a_E = 160$. Such low threshold values are due to extreme focusing and *ponderomotive trapping* near the central point. Particles are confined for some time in the vicinity of the central point by the well-like ponderomotive potential, and they can accumulate influence of radiative effects. At such powers in the e-dipole wave (which features a hill-like ponderomotive potential near the center) particles quickly leave the focal region, so ART is observed only at much greater powers [53].

The ART regime in the power range $P_1 < P < P_2$ (0.1 PW $< P <$ 1 PW) increases the relative number of particles between the first node and the first antinode of the electric field [see Figs. 3(a) and 3(b)]. This causes a rise of the relative number of particles which can gain large energy in the region of strong electric field. This rise is confirmed by the shift of the left edge of $\overline{W}'_{\varepsilon_r}$ to larger ε_r in Fig. 3(e). At the same time the ART regime leads to an increase of the angle of particle escape with respect to the z axis [see Figs. 3(c) and 3(d)] and few particles can escape the focal region in transverse directions, $60° < \theta < 120°$. During such an escape accelerated particles cross regions with the strong magnetic field (regions of the electric field nodes) and can experience noticeable radiation losses. As a result, when the wave power approaches $P = P_2$, the location of the maximum of the averaged *relative spectrum* begins to shift to lower ε_r from $\varepsilon_{r,m} \approx 0.6$ [see Figs. 3(e) and 3(f)].

At powers $P > P_2 = 1$ PW the so-called *normal radiative trapping* (NRT) [33,50,55] appears and the relative number of particles in the vicinity of the second electric field node increases [see Figs. 3(a) and 3(b)]. Particles passing through the region of the second node of the electric field have a high probability to emit a hard photon. Such an emission significantly increases curvature of motion, and particles start oscillating around the electric field node for some time, i.e., the

particle becomes trapped. Due to hard photon emission the maximum of $\overline{W}'_{\varepsilon_r}$ is shifted to lower normalized energies ε_r and quite a good [according to Figs. 3(e) and 3(f)] approximation for the location of the maximum in a wide range of powers 1 PW $< P <$ 300 PW can be found:

$$\varepsilon_{r,m} \approx 0.5 P_{\mathrm{PW}}^{-0.48}. \qquad (8)$$

Together with Eqs. (2) and (7) this approximation is evidence that the energy (without the normalization) of the majority of escaping particles ε_m becomes almost independent of wave power. In the range 1 PW $< P <$ 300 PW ε_m is from $250mc^2$ to $350mc^2$ (from 130 to 180 MeV). Also in the range 1 PW $< P <$ 135 PW although higher power leads to a broader energy distribution of escaping particles as function of ε, this broadening is quite small. This corresponds to preservation of the width of $\overline{W}'_{\varepsilon_r}(\varepsilon_r)$ on a logarithmic scale [see Figs. 3(e) and 3(f)].

At the same time in the power range $P_2 < P < P_3$ (1 PW $< P <$ 8 PW) ART becomes more prominent. Stronger radiation losses in this power range can impede particle escape even from the region $\rho_m < \rho < 0.45\lambda$ where without photon recoil $\overline{n}$ nearly vanishes. As a result, the additional maximum of $\overline{n}$ appears within $0.2\lambda < \rho < 0.4\lambda$ [see Figs. 3(a) and 3(b)]. Also due to the stronger radiation losses the portion of particles leaving the focal region at $60° < \theta < 120°$ significantly increases [see Figs. 3(c) and 3(d)].

At powers $P_3 < P < P_4$ (8 PW $< P <$ 25 PW) the set of the possible regimes of motion is the same as the one at $P_2 < P < P_3$: *ponderomotive trapping* (*ponderomotive escape*), ART and NRT. However, at time $t = t^*$, when the regimes of motion become steady state, the NRT regime becomes dominant, so the relative number of particles moving in the ART regime noticeably decreases. This can be seen as the reduction of $\overline{n}$ in the range $0.05\lambda < \rho < 0.45\lambda$ and by its rise in the range $0.5\lambda < \rho < 0.9\lambda$ [Figs. 3(a) and 3(b)]. Due to particle redistribution between the regimes of motion regions of polar angle $0° < \theta < 25°$ and $155° < \theta < 180°$ appear to be more populated [Figs. 3(c) and 3(d)].

At powers $P_4 < P < P_5$ (25 PW $< P <$ 135 PW) a new ART regime emerges in the region $0.45\lambda < \rho < 0.6\lambda$, while the ART regime discussed above decreases its impact on $\overline{n}$ within the region $0.05\lambda < \rho < 0.45\lambda$ sufficiently [see Figs. 3(a) and 3(b)]. Based on trajectory analysis it will be shown in Sec. III E that these ART regimes feature different traits of motion. The region $0.45\lambda < \rho < 0.6\lambda$ corresponding to the new ART regime becomes more populated by particles, and at $P > 70$ PW this results in an additional maximum of $\overline{n}$ at $\rho \approx 0.55\lambda$. *Ponderomotive trapping* and NRT regimes exist in this power range and result in the maxima of $\overline{n}$ at $\rho = 0$ and $\rho \approx 0.72\lambda$, respectively.

The averaged *relative spectrum* does not differ qualitatively and exhibits the same behavior as for lower powers: the width is approximately constant and the location of the maximum is described by Eq. (8) [see Figs. 3(e) and 3(f)]. The reduction of the normalized energy of escaping particles can be explained by radiation losses in regions of the NRT regime where the magnetic field is quite strong and stimulates photon emission. However, there are changes in the averaged angular characteristic $\overline{W}'_\Omega$. First, it becomes nonmonotonic in the ranges

$0° < \theta < 45°$ and $135° < \theta < 180°$, and in each region two maxima appear. Second, $\overline{W}'_\Omega$ in the region $45° < \theta < 135°$ is less than for lower powers $P_2 < P < P_4$ [see Figs. 3(c) and 3(d)].

At powers $P > P_5$ ($P > 135$ PW) the *ponderomotive trapping* regime is considerably suppressed, which can be seen from the near disappearance of the maximum in the center ($\rho = 0$); see Figs. 3(a) and 3(b). Energy and angular distributions obtain specific features. The averaged energy spectrum is wider, which is especially clear at the tails of $\overline{W}'_{\varepsilon_r}$. A comment on this broadening of the energy spectrum is given in Sec. F of the Supplemental Material [56]. Nevertheless, the location of the maximum is in accordance with the approximation in Eq. (8) [see Figs. 3(e) and 3(f)]. A portion of the particles escapes the focal region preferably transversely to the z axis and one of the maxima of $\overline{W}'_\Omega$ lies at $\theta = 90°$ [see Figs. 3(c) and 3(d)]. At $P > 250$ PW transverse escape is primary. The reason behind such changes will be analyzed in the next section.

Thus, the introduced averaged characteristics can be considered as indicators of radiative effects. Joint analysis of these characteristics allows distinguishing five threshold powers which separate different dynamics of the particle ensemble. These changes can be caused by the emergence of new regimes of motion and the redistribution of particles between these regimes. Proposed characteristics provide a general view on particle motion at the macrolevel, while the necessity of comprehension of particle trajectories remains.

E. Analysis of particle trajectories

Analysis of individual particle motion is necessary in order to understand the observed macrocharacteristics and explore properties of different regimes hidden at the macrolevel. In this section we consider particle trajectories observed during the evolution of ensembles of electrons and positrons described in Sec. III D in the identified ranges of wave power. In each performed simulation we have saved 2×10^4 trajectories of initially at-rest electrons and positrons distributed uniformly within a sphere with radius 0.6λ with the center in the central point. Fields are set analytically according to Eq. (1). The rest of the parameters of simulations are described in Sec. III B.

Simulations show that motion in fields of the standing m-dipole wave is chaotic due to two reasons. The first reason is the stochasticity of photon emission. The second reason is the divergence of phase-space trajectories of initially closely located particles moving in fields of a standing wave [57,58]. This reason plays a key role in the chaotization of particle motion between acts of photon emission or when photon recoil can be neglected.

Even though particle motion is chaotic, an analysis of trajectories can be informative and allow distinguishing and understanding different regimes of motion. Similarly to the cases of plane standing waves [32] and more general field configurations [59], our simulations show that trajectories in the case of the standing m-dipole wave with and without photon recoil taken into account consist of parts formed in different spatiotemporal regions: electric and magnetic, where electric or magnetic fields dominate. According to simulations, within
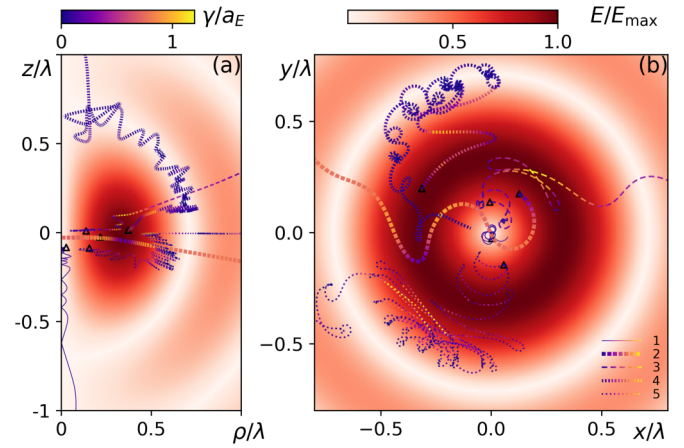

FIG. 4. (a) Key types of trajectories corresponding to different power ranges in fields of the m-dipole wave in plane $z\rho$ and (b) projections of the trajectories onto the central xy plane. Numbered trajectories from 1 to 5 are obtained at wave powers 0.04, 0.04, 4, 16, and 200 PW, respectively. Triangles show starting points of trajectories. Colors along trajectories denote Lorentz factor values. The electric field distribution is shown in shades of red (gray).

any one of these regions trajectories that are close in the phase space are qualitatively similar and mainly diverge as a result of transition between these regions. So the characteristic time of divergence is close to a multiple of $0.5T$. This time of divergence is sufficient to study the dynamics of the particle ensemble over several half-periods and reveal common features of particle motion in different regimes. Also we would like to draw attention to the following fact. Spatial, energy, and angular particle distributions obtained in Sec. III D depend smoothly on wave power, meaning that a considerable number of particles change their motion depending on power in a certain similar way which can be detected.

In order to analyze trajectories, for each wave power we divide saved trajectories into several groups based on initial particle location, time interval before escape, direction of escape and the region (the antinode or the node of the electric field) from where particles have escaped. Trajectories in each group turn out qualitatively similar each other. In order not to distract the reader, a detailed comparison of trajectories in these groups at different wave powers is presented in the Supplemental Material [56], where we also consider how they determine the time in the trapped state (*trapping time*), spatial, energy, and angular distributions in different regimes of motion. Below we discuss six key types of trajectories in the revealed power ranges (see Fig. 4).

The first type of trajectories demonstrates *ponderomotive trapping* which in the power range $P < 0.1$ PW is the most typical. Radiative effects in this power range are negligible, and particle motion is mainly determined by field gradients. Particles within the region constrained by the first electric field antinode (the central region) oscillate in azimuthal and radial directions like in a ponderomotive potential and drift mainly along the z axis due to field inhomogeneity (trajectory 1 in Fig. 4). In simulations we have found such trajectories up to $P = P_5 = 135$ PW. These trajectories explain the maximum

at $\rho \approx 0$ of the obtained average spatial distribution at $P < P_5$ [Figs. 3(a) and 3(b)].

The second type of trajectories is a result of a specific feature of the m-dipole wave. The azimuthal electric field causes particle rotation, and the centrifugal force can release particles from *ponderomotive trapping*, pushing them out of the central region (trajectory 2 in Fig. 4). A simple estimate based on the balance of Lorentz and centrifugal forces from Eq. (4) shows that a particle can be released from trapping at the distance

$$\rho_b = \sqrt{2.5}\lambda/2\pi \approx 0.25\lambda \qquad (9)$$

from the axis of field symmetry (z axis). Derivation of the estimate is given in Appendix B. Although it is quite a rough estimate, the value of ρ_b is in agreement with the averaged spatial distribution of particles [see Figs. 3(a) and 3(b)], which shows that their largest portion is within the region $\rho \lesssim 0.1\lambda$.

The described trajectories explain well the angular and energy distributions obtained from numerical simulations [see Figs. 3(c)–3(f)] up to $P < P_2$ ($P < 1$ PW). *Ponderomotively trapped* particles escape mainly along the z axis and have relatively low energy. Particles pushed out of the central region contribute to the angular distributions at $0° < \theta < 45°$ and $135° < \theta < 180°$. Also, since during escape particles can cross the antinode region and radiation losses are negligible in this power range, their normalized energy can be comparable with $\varepsilon_r = 1$.

The third type of trajectories shows *ponderomotive escape* of particles initially located between the first antinode and the second node of the electric field. This escape from the focal region happens over a short period of time (within half a wave period) in the direction determined by field gradients. This regime is mostly observed in the power range $P < P_3 = 8$ PW. However, it can also be detected at larger powers, but, more likely, a particle which is going to escape will be trapped owing to radiative effects. Due to the quick escape of particles in this regime, they do not contribute to the averaged distributions ($\overline{n}, \overline{W}'_\Omega, \overline{W}'_{\varepsilon_r}$) discussed in the previous section. The part of trajectory 2 in Fig. 4 outside the location of the first electric field antinode ($\rho > \rho_m = 0.33\lambda$) is similar to trajectories in the regime of *ponderomotive escape*. In order not to overfill Fig. 4, examples of trajectories corresponding to this regime are given in the Supplemental Material [56] (see trajectory 3 in Figs. 1–3).

The fourth type of trajectories demonstrates the influence of radiative effects and represents the ART type of trajectories (trajectory 3 in Fig. 4). Radiative effects become significant at powers $P > P_1$ ($P > 0.1$ PW) and cause a growth of the time of particle escape [see Fig. 2(d)]. Some of the particles initially located close to the z axis can be attracted to the region of the strongest electric field. During their approach to the electric field antinode particles make a shift in the radial direction each half of wave period. In the region of the ART regime when the electric field exceeds the magnetic field, particles are accelerated mainly along the electric field (along the azimuth). After this, when the magnetic field exceeds the electric field, particles make a turn, losing a significant part of the previously gained energy to photon emission. At the next half of wave period particles are again accelerated along

the electric field, but in the opposite azimuthal direction and closer to the antinode. Moreover, radiation losses counteract the dominance of the centrifugal force, so particles can oscillate in the vicinity of the electric field antinode (where $\rho > \rho_b$) for several half-periods before escaping this region. Such eight-like motion is similar to particle motion in the ART regime in fields of the e-dipole wave [22,43] but at greater powers, $P > 10$ PW. Emergence of the ART regime explains the growth of $\overline{n}$ in the region $0.05\lambda < \rho < 0.45\lambda$ [see Figs. 3(a) and 3(b)] and the slight decrease of the relative number of low energetic particles [Figs. 3(e) and 3(f)] at $P_1 < P < P_3$ (0.1 PW $< P < 8$ PW). Also radiation losses enhanced in the ART regime slows down axial drift (along the z axis) caused by field inhomogeneity, thus stimulating the particle escape within the angular range $10° < \theta < 170°$ at $P_1 < P < P_4$ (0.1 PW $< P < 25$ PW); see Figs. 3(c) and 3(d).

The fifth type of trajectories is related to another radiative regime called NRT, which is observed at powers $P > P_2$ ($P > 1$ PW); see trajectory 4 in Fig. 4. Particles moving in this regime are trapped and accumulated in the region of the second electric field node due to radiation losses [see Figs. 3(a) and 3(b)]. Note that even highly energetic particles passing through this region may become trapped in the NRT regime due to significant energy losses (see trajectory 4 in Fig. 4). In contrast, particles can become ponderomotively trapped only if they are initially located very close to the second electric field node. So at $P > P_2$ NRT ensures a clear maximum of the averaged spatial distribution of particles at the position of the second electric field node in the vicinity of the central plane ($\rho \approx 0.72\lambda$); see Figs. 3(a) and 3(b). When trapped, particles drift along the sphere corresponding to the second electric field node (the sphere of the node) and gyrate in the strong magnetic field. The radius of rotations oscillates depending on the instantaneous magnetic fields and accumulated energy.

In order to be trapped in the NRT regime, particles should lose a significant part of their energy, and afterwards they cannot reach the maximal energy $\varepsilon_{r,m}$ gained earlier in the region of the first electric field antinode. Thus, NRT is the main reason of energy decrease of escaping particles at $P > P_2$ [see Figs. 3(e) and 3(f)]. At $P > P_3$ ($P > 8$ PW) NRT becomes much more probable for the particles escaping the antinode region, also *trapping time* (time in the trapped state) increases significantly. During the drift particles can reach the top of the sphere of the node at $|z| \approx 0.7\lambda$ and escape close to the z axis at polar angles in the ranges $0° < \theta < 25°$ and $155° < \theta < 180°$ [see Figs. 3(c) and 3(d)].

We would like to note that at powers above $P \approx P_2 = 1$ PW the quantum effects of photon emission significantly influence particle distributions. Radiation losses should be considered random acts of photon emission and the power of photon emission should be corrected [60]. The quantum approach employed in our simulations includes both of these factors. The quantum impact is determined by the dimensionless quantum parameter [34]

$$\chi = \eta\sqrt{\{\varepsilon\mathbf{E}/(mc^2) + [\mathbf{p}/(mc) \times \mathbf{B}]\}^2 - (\mathbf{E} \cdot \mathbf{p})^2/(mc)^2}, \qquad (10)$$

where $\eta = \hbar\omega/(mc^2) \approx 2.7 \times 10^{-6}$ and fields are dimensionless. This parameter can be largest along the trajectories of particles which gain energy in the region of strong electric

field and then turn in a strong magnetic field region or crossing this region (for example, the beginning of the trajectory 4 in Fig. 4). Indeed, assuming an accumulated energy of about $a_E mc^2$ and a strong magnetic field of about $0.34a$ [see Fig. 1(b)], the maximal value of χ is about

$$\chi_{\max} \approx 0.34 \eta a_E a \approx 0.4 P_{\text{PW}}. \tag{11}$$

Quantum effects becomes important when $\chi \gtrsim 1$, so, at $P \gtrsim P_2$.

The sixth type of trajectories (trajectory 5 in Fig. 4) corresponds to one more intriguing ART regime emerging in highly inhomogeneous fields of the m-dipole wave at $P > P_4$ ($P > 25$ PW). The distinctive feature of this trapping regime is that due to radiation losses particles are not only constrained in the radial direction between the second node and the first antinode of the electric field but also attracted to the central plane ($z = 0$). This attraction manifests itself in the change of an outwards drift with respect to this plane to a drift towards this plane. This radiative regime can also be called *anomalous* because such trapping contradicts the dynamics dictated by the ponderomotive potential.

The first ART regime emerging at $P > P_1$ ($P > 0.1$ PW) is characterized mainly by radial attraction to the electric field antinode, so we name it *radial* ART. The second ART regime is distinguished by axial drift towards the central plane, and we name this regime *axial* ART. Trajectories show (for example, trajectory 5 in Fig. 4) that even if initially particles are attracted in the radial direction to the electric field antinode and are going to escape the focal region due to axial drift (i.e., move in *radial* ART), they can be retrapped. As a result, they are attracted to the central plane and start oscillating in the range $0.45\lambda < \rho < 0.6\lambda$. In this range of ρ such motion leads to formation of a local maximum of the averaged spatial distribution of particles at $P > 70$ PW [see Figs. 3(a) and 3(b)].

In the power range $P_4 < P < P_5$ (25 PW $< P < 135$ PW) *axial* ART does not dominate, *trapping time* in this regime is not large enough to attract a lot of particles to the central plane. As a result, there is no clear signature of this regime in the averaged angular distribution [see Figs. 3(c) and 3(d)]. Moreover, particles released from *axial* ART can be retrapped in NRT, then they drift to the top of the sphere of the node and finally escape the focal region close to the z axis. However, at $P > P_5$ the probability of trapping in the *axial* ART regime, as well as *trapping time*, increases significantly, and the local maximum of the averaged angular distribution at $\theta = 90°$ appears.

Also we would like to emphasize the uniqueness of the *axial* ART regime. If radiation losses are considered as a damping force (Landau-Lifshitz force [26] or Landau-Lifshitz force with a quantum correction [50]) an attractor is formed in highly inhomogeneous fields of the m-dipole wave in the central plane at a distance of $\rho \approx 0.55\lambda$. Thus, only stochasticity of photon emission breaks the attractor in the *axial* ART regime and limits *trapping time*. Note that in the case of the e-dipole wave there is no attractor: although particles are attracted to the axis of symmetry in the radial direction in the ART regime, they eventually escape the focal region in the axial direction even if radiation losses are taken into account as a continuous force.

Since the time of particle escape from the focal region t_{10} becomes mainly determined by *trapping time* in the *axial* ART regime at $P \gg P_4$ ($P \gg 25$ PW) and since this *trapping time* is limited due to the stochasticity of photon emission, based on properties of motion in this regime and the probability of photon emission we can fit $t_{10}(P)$ by the function

$$\bar{t}_{10}(P > 25 \text{ PW}) = \frac{0.5 \ln(0.1)T}{\ln\left[1 - \exp\left(-0.18 P_{\text{PW}}^{0.49}\right)\right]}$$
$$\approx \frac{-1.15T}{\ln\left[1 - \exp\left(-2.6 \times 10^{-4} a^{0.98}\right)\right]}. \tag{12}$$

The derivation of $\bar{t}_{10}(P)$ is given in the Appendix C. This fitting shown in Fig. 2(d) by the dash-dotted line is in good agreement with the numerical results. Moreover, according to Eq. (12) at powers $P \gg P_4$ the time of escape demonstrates exponential growth with an increase in field amplitude:

$$\bar{t}_{10} \approx 1.15T \exp\left(0.18 P^{0.49}\right) = 1.15T \exp\left(2.6 \times 10^{-4} a^{0.98}\right). \tag{13}$$

Note that in the case of the e-dipole wave at powers $P \gg 25$ PW the escape time is proportional to $P_{\text{PW}}^{0.17}$ [53]. Such a difference is observed because in the e-dipole wave ART is not as strong and particles escape from the trapped state even without stochasticity of photon emission.

In order to summarize Secs. III C–III E we review the obtained results. Based on the analysis of trajectories, the escape time and the averaged particle distributions we have revealed different power thresholds. The revealed thresholds are determined not only by the emergence of new regimes of motion, but also by the redistribution of particles between the different regimes. The possible regimes of motion are the following. At powers $P < P_1 = 0.1$ PW radiation losses are negligible; *ponderomotive trapping* and *ponderomotive escape* are the main regimes. At $P \approx P_1$ *radial* ART emerges. Such a low-power threshold is caused by the specific field structure in which particles can be ponderomotively trapped in the strong field region even without radiative effects. NRT appears at $P \approx P_2 = 1$ PW, and *axial* ART becomes possible at $P \approx P_4 = 25$ PW. Since field structures are nonsymmetric with respect to the surface crossing the electric field antinode and parallel to the z axis, the ART regimes are different in different regions. In the vicinity of the antinode closer to the central point particles can move in the *radial* ART regime, experiencing radial attraction to the antinode and axial drift outwards from the central plane. On the other side of the surface particles can move in the *axial* ART regime, oscillating between the second node and the first antinode and getting attracted to the central plane. In *axial* ART an attractor is almost formed, but is prevented by randomness of photon emission. This results in quite a steep dependence of *trapping time* and escape time on wave power. Both ART regimes favors transverse particle escape with respect to the z axis, while the NRT regime leads to axial particle escape and causes the reduction of the normalized energy of escaping particles.

F. Energy and angular spectra of photons

From the practical point of view it is also important to determine the angular and energy characteristics of generated gamma photons. A significant part of total photon energy is
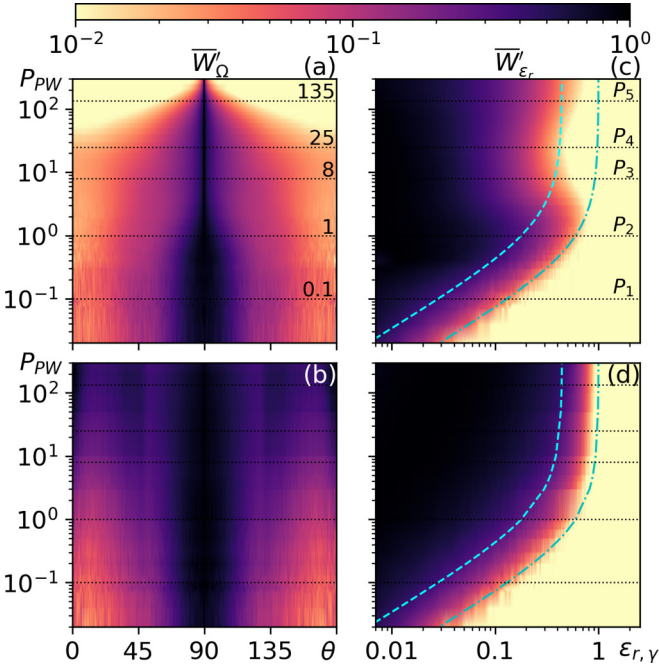
FIG. 5. Maps of (a), (b) averaged angular distribution $\overline{W}'_\Omega$ and (c), (d) averaged *relative spectrum* $\overline{W}'_{\varepsilon_r}$ of generated gamma photons escaping the observation sphere. For comparison we present results obtained (a), (c) with and (b), (d) without photon recoil taken into account. Horizontal black dotted lines show previously determined power thresholds. Estimates of characteristic normalized energies of photons $\varepsilon_{r,\gamma}^{\mathrm{cut}}$ and $\varepsilon_{r,\gamma}^{\mathrm{cut2}}$ emitted by particles with maximal possible and half of maximal possible energies as functions of P are shown by dash-dotted and dashed lines in (c) and (d), respectively.

emitted while particles oscillate in the region of strong fields, moreover photons propagate along straight lines, so they can be good characteristics of particle motion in the focus. In order to characterize escaping photons we use expressions for $\overline{W}'_\Omega$ and $\overline{W}'_{\varepsilon_r}$ introduced in Sec. III D (and Appendix A), but we replace particle characteristics (momentum and energy) with those of the photon. Unlike the angular particle distribution and the particle *relative spectrum*, the same characteristics for photons change with increasing power even without photon recoil. For example, although photon escape is mainly transverse in the whole power range without (as well as with) photon recoil [see Figs. 5(a) and 5(b)], the angular spread increases with increasing power [see Fig. 5(b)].

For the process of photon emission the key parameters are the particle's energy and dimensionless quantum parameter χ, which determines the probability of photon emission and the photon spectrum. Though analytical derivation of the photon spectrum is challenging, it is possible to estimate the cutoff of normalized photon energy $\varepsilon_{r,\gamma}^{\mathrm{cut}}$. The maximal possible particle energy is approximately $\varepsilon^{\mathrm{cut}} = a_E m c^2$, the maximal transverse field is around a, so, according to Eqs. (2) and (10), $\chi^{\mathrm{cut}} \approx \eta a a_E \approx 1.1 P_{\mathrm{PW}}$. The characteristic normalized photon energy emitted by a particle with $\varepsilon^{\mathrm{cut}}$ and χ^{cut} can be estimated according to Ref. [60] as

$$\varepsilon_{r,\gamma}^{\mathrm{cut}} \approx \chi^{\mathrm{cut}}/(2/3 + \chi^{\mathrm{cut}}) \approx 1.1 P_{\mathrm{PW}}/(2/3 + 1.1 P_{\mathrm{PW}}). \quad (14)$$

For visualization we also show the characteristic normalized energy of photons emitted by particles with a twice lower energy in the same fields: $\varepsilon_{r,\gamma}^{\mathrm{cut2}} \approx 0.25\chi^{\mathrm{cut}}/(2/3 + 0.5\chi^{\mathrm{cut}}) \approx 0.27 P_{\mathrm{PW}}/(2/3 + 0.55 P_{\mathrm{PW}})$.

In the power range $P < P_1 = 0.1$ PW angular and energy characteristics with and without photon recoil are very similar (see Fig. 5), cutoff energies are well approximated by Eq. (14) [see Figs. 5(c) and 5(d)]. Normalized photon energy grows almost linearly with increasing power. Photons escape the focal region at polar angles $70° < \theta < 110°$. Since photons with the greatest energy are emitted in the vicinity of the central plane, where axial drift is relatively slow and the main components of motion are radial and azimuthal, the maximum of averaged angular characteristics of photons is at $\theta = 90°$. This conclusion is relevant for the whole power range and does not depend on photon recoil.

In the power range $P_1 < P < P_2$ (0.1 PW $< P < 1$ PW) changes caused by radiation losses become noticeable. When photon recoil is allowed for, the angular spread begins to shrink; see Fig. 5(a). The situation is opposite when we do not take into account photon recoil [Fig. 5(b)]: in this case particle trajectories do not change with increasing power, but ε and χ increase. This enhances emission of photons with a greater part of particle energy at different moments, including those when the particle momentum and the z axis are far from perpendicular. As a result, the angular spread of gamma radiation becomes wider.

This conclusion is not applicable in the case when photon recoil is allowed for. The parts of a trajectory where photon emission is more probable become more and more important with increasing power. The reason is that the greater the power, the greater portion of energy a particle loses in an act of photon emission on average, and consequently, the larger the increase of trajectory curvature. Thus, the trajectory transforms, and this transformation happens in such a way that segments of the trajectory where photon emission is stimulated or suppressed can be distinguished. Particularly, in the considered power range this leads to the emergence of *radial* ART, which causes photon recoil to become more noticeable. Photon recoil is directed approximately opposite to the particle momentum in the ultrarelativistic case [26]; as a result radiation losses slow down axial drift, and particles can obtain smaller axial momentum. This enhances photon emission in the transverse direction with respect to the z axis [compare Figs. 5(a) and 5(b)]. Also, although radiation losses should lead to dissipation, the number of energetic photons with normalized energies $0.01 < \varepsilon_{r,\gamma} < 0.1$ increases due to *radial* ART [compare Figs. 5(c) and 5(d)].

At greater powers the angular spread of escaping photons decreases and becomes around 1° at $P = 300$ PW [Fig. 5(a)]. This is mainly related to the slowing down of axial drift. Note that without photon recoil the energy distribution is much wider at powers $P \gg P_2 = 1$ PW.

The energy characteristic shows more variations. In the range $P_2 \lesssim P \lesssim P_4$ (1 PW $\lesssim P \lesssim 25$ PW), while without photon recoil normalized photon energies reach almost maximal possible values, radiation losses lead to a decrease of photon energies. This is clearly visible if the edge of the

averaged *relative spectrum* $\overline{W}'_{\varepsilon_r}$ is compared with $\varepsilon_{r,\gamma}^{\text{cut}}$ and $\varepsilon_{r,\gamma}^{\text{cut2}}$ [Figs. 5(c) and 5(d)]. The emerging NRT is the reason of this decrease. When *axial* ART emerges at $P \gtrsim P_4$, normalized photon energies increase and reach almost maximal possible values $\varepsilon_{r,\gamma}^{\text{cut}}$.

Thus, we show that in the standing m-dipole wave generated photons propagate in the transverse direction and the angular spread decreases from $40°$ at $P = 0.01$ PW up to $1°$ at $P = 300$ PW. Although the angular distribution does not allow clear distinguishing of thresholds of *radiative trapping* regimes, at $P > 1$ PW it becomes significantly narrower due to radiation losses in comparison with the one obtained without photon recoil. However, if we consider the angular distribution together with the energy distribution, power thresholds of ART and NRT regimes can be determined. The dominant regime of particle motion substantially influences the cutoff value of the energy distribution. When ART regimes are strong, the cutoff energy can be around the maximal particle energy $a_E mc^2$. In the NRT regime the cutoff energy is up to 2 times lower. The average photon energy is more than an order of magnitude lower and is in the range $(0.01–0.1)a_E mc^2$ in *radiative trapping* regimes.

IV. EXPERIMENTAL SIGNATURE OF RADIATION FRICTION EFFECT

In the recent years, with the advent of superpowerful lasers, there has been a lot of fundamental investigations devoted to experimental testing of the quantum nature of radiative effects in the dynamics of relativistic particles (see, e.g., Refs. [47,48,61]). The main attention was paid to the case of combined use of high-power lasers and relativistic electron beams moving towards the laser wave, since in this case their interaction is the most extreme from the quantum point of view. Due to the Lorentz transformation, the frequency of scattered photons increases by a factor of $4\gamma^2$, where γ is the relativistic gamma factor. However, results presented above show that at laser powers of only about $P_1 = 0.1$ PW, which are available in many laboratories [1], particle dynamics in the m-dipole wave can be strongly affected by radiative effects. Thus, angular and energy distributions of escaping particles and generated photons allow distinguishing cases with and without radiation losses. Moreover, according to Eq. (11) in the petawatt range of powers quantum effects become important. So here we would like to propose an all-optical experiment to shed light on the quantum nature of the radiation friction effect: irradiation of a target by petawatt laser radiation focused in the form of a converging m-dipole wave. In experiments the m-dipole wave can be closely mimicked by a number of linearly polarized beams [24,33].

In order to show the fundamental possibility of such experiments we use the PIC code PICADOR to study numerically the interaction of a test hydrogen-like target in the form of a nanowire with radius 0.25λ and density $n_0 = 10 n_{\text{cr}}$, where $n_{\text{cr}} = m\omega^2/(4\pi e^2) \approx 1.4 \times 10^{21}$ cm^{-3} with an ideal m-dipole wave with a peak power of $P = 3$ PW with a $\sin^2$ envelope and a FWHM duration of 30 fs. We compare the resulting spectra of particles and photons in three cases: when photon recoil is omitted and when photon emission is considered within classical and quantum approaches. The last approach is

described in Sec. III B. Within the classical approach radiation losses are taken into account as a force in the Landau-Lifshitz (LL) form [26].

The simulation box is sized $6\lambda \times 6\lambda \times 6\lambda$ and the number of cells is $768 \times 768 \times 768$ along x, y and z axes, the time step is $dt = T/300$. The target is aligned along the wave symmetry axis (z axis) and the initial number of particles of each type (electrons and ions) is 1.2×10^7. Unlike the simulations described in the previous sections, here the laser-plasma dynamics is considered self-consistently. The dipole wave is generated as described in Refs. [22,24,25]; particles influence fields through generated currents, for which the FDTD method [62] is employed. Note that the process of photon decay is also included in simulations but the rate of pair creation is slow at the considered wave power and generated pairs do not affect the laser-plasma interaction.

Initially fields of the converging m-dipole wave cannot penetrate deep into plasma. Up to $t \approx 10T$ the maximal dimensionless electric field $|E|^{\text{max}}$ is less, or even much less, than the maximal electron density $n_{e^-}^{\text{max}}$ normalized to the critical density n_{cr} [see Fig. 6(a)], so plasma is relativistically overcritical and opaque. However the incident radiation excites boundary oscillations at the doubled laser frequency and causes plasma compression. These oscillations and the compression are evident [see Fig. 6(b)] from the temporal evolution of the average radius of the electron distribution $r_{e^-}^{\text{av}} = \iiint_{V_c} \rho n_{e^-} d^3\mathbf{r}/N_{e^-}^c$ within the central region V_c ($\rho, |z| < 0.33\lambda$), where $N_{e^-}^c$ is the total number of electrons in this region. At the moment $t \approx 7.2$ T electrons become maximally compressed into a wire with the average radius $r_{e^-}^{\text{av}} \approx 0.04\lambda$ and maximal density $\approx 600 n_{\text{cr}}$ [see Fig. 6(c)]. In turn, ions, being much heavier, are not as mobile as electrons, so the compression of electrons induces a strong radial electric field [E_x in Fig. 6(c)] due to charge separation. When the maximal electron compression is achieved this field becomes strong in comparison with the wave's (azimuthal) electric field [E_y in Fig. 6(c)] and increases the radial scale of the electron column up to $r_{e^-}^{\text{av}} \approx 0.1\lambda$ [Fig. 6(b)]. While $t \lesssim 10T$, the field intensity in plasma is insufficient to initiate the radiation-dominated regime and there is no difference in plasma-field dynamics within various approaches to the description of radiative effects. So Fig. 6(a) up to $t \approx 10T$ as well as Fig. 6(c) are relevant for all considered approaches.

However, at $t \gtrsim 10T$, due to the increase of the field amplitude of the incident pulse, the field of charge separation can be neglected in comparison with the wave fields [see Fig. 6(d)], so particle dynamics becomes very similar to particle dynamics in given fields [see Figs. 3(a) and 3(b)]. Since at this stage fields penetrating into plasma correspond to the wave power greater than $P_1 = 0.1$ PW, the difference in spatial distributions with and without photon recoil emerges [see Figs. 6(b) and 6(d)–6(f)] in accordance with the results presented in Sec. III D. After $t \approx 12.5T$ the instantaneous power $\gtrsim 1$ PW, $\chi_{\text{max}} \gtrsim 1$ [see Eq. (11)], so the difference between LL and quantum approaches becomes visible. As follows from Fig. 3(a), the greater the wave power, the stronger the radiation losses and the larger the radial scale of the electron distribution due to an increasing portion of particles moving in the *radial* ART regime. Since the LL approach overestimates radiation losses, this approach makes the *radial* ART regime
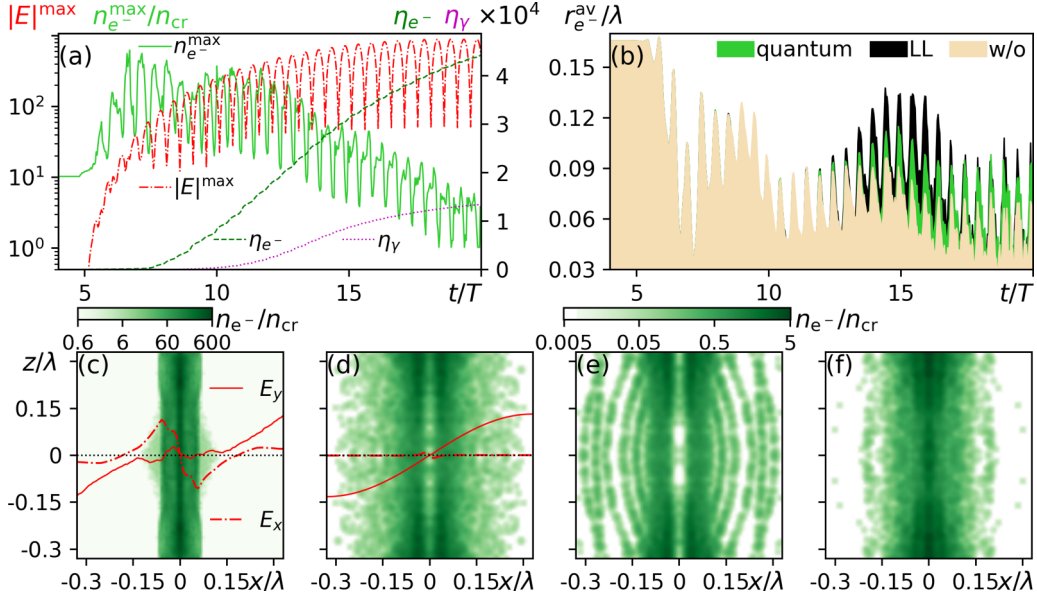
FIG. 6. Dynamics of the electric field and electrons within the central region as a result of irradiation of a cylindrical target with radius 0.25λ and density $10n_{cr}$ by the converging pulsed m-dipole wave with peak power 3 PW and FWHM pulse duration of 30 fs. (a) Temporal evolution of maximal dimensionless electric field $|E|^{max}$, maximal electron density $n_{e^-}^{max}$ normalized to the critical density n_{cr}, efficiencies of transformation of laser energy into energy of escaping electrons η_{e^-} and into energy of gamma radiation η_γ within the quantum approach for description of radiative effects. (b) Comparison of temporal evolution of $r_{e^-}^{av}$ (the average distance of electrons from the axis of symmetry divided by the wavelength) in cases when radiative effects are omitted (w/o) and when they are taken into account within the quantum or classical Landau-Lifshitz (LL) approaches. (c) Electron distribution at $t = 7.2T$ corresponding to the maximal compression of electrons in quantum case. (d–f) Electron distributions at $t = 14.4$ T corresponding to transparent plasma in the quantum case, in the case of the classic radiation losses in the LL form and in the case without radiative effects, respectively. For all three cases the color bar is the same and is above panel (e). Solid and dash-dotted lines in panels (c) and (d) demonstrate comparative distributions of electric filed components E_y an E_x normalized to the maximum of $|E_y|$ along the x axis, respectively. Horizontal thin dotted lines in panels (c) and (d) correspond to $E_{x,y} = 0$.

more prominent and leads to a larger scale of the radial electron distribution [see Fig. 6(e)] in comparison with the scale of the distribution in the quantum approach [see Fig. 6(d)] or in the approach omitting radiative recoil [see Fig. 6(f)]. Here and below this overestimation means that the power of emitted radiation given by the classical model is greater than the quantum power of radiation at the same conditions [60]. Such a relation between various approaches is also confirmed by the evolution of $r_{e^-}^{av}$ [see Fig. 6(b)]. These specific features of spatial distributions within different approaches determine distinctive characteristics of the generated gamma photons and escaping electrons and positrons.

In order to reveal signatures of radiative effects, in the case of a pulsed wave we propose to use energy and angular characteristics very similar to those introduced in Sec. III D (and Appendix A) but without averaging. We take into account escaping particles and photons crossing the observation sphere with the radius of $r_{obs} = 3\lambda$ during the whole simulation time, not only for a number of wave periods after $t = t^*$. The angular distribution E'_Ω denotes the total energy of particles or photons having crossed the observation sphere with momentum directed into an element of solid angle $d\Omega$ in the momentum space. *Relative spectrum* E'_{ε_r} denotes the total energy of particles or photons having crossed the observation sphere with energy in range from ε_r to $\varepsilon_r + d\varepsilon_r$. In Fig. 7 these characteristics normalized to their maxima $\overline{E}'_\Omega = E'_\Omega/E'^{max}_\Omega$ and $\overline{E}'_{\varepsilon_r} = E'_{\varepsilon_r}/E'^{max}_{\varepsilon_r}$ are presented.

Note, that the largest portion of escaping particles and photons characterizes the stage of particle motion in the given field (considered in previous sections), when plasma fields can be neglected. In order to demonstrate this finding we present in Fig. 6(a) the evolution of transformation efficiencies of the laser energy into the energy of escaping particles η_{e^-} and gamma photons η_γ. The efficiency is equal to the total energy of electrons or photons, which have crossed the observation sphere before a given moment of time, divided by the total energy of the laser pulse. Escaping particles and most generated gamma photons need approximately $t_d \approx 3T$ to reach the observation sphere (discussed above in Sec. III D), so in Fig. 6(a) curves η_{e^-} and η_γ are shifted to the left by t_d. The efficiency η_{e^-} shows that the energy of the gamma photons generated before the end of the stage of self-consistent laser-target interaction ($t = 10T$) constitutes 3% of the total energy of gamma photons generated during the whole interaction. For electrons this ratio is 17%. Moreover, at $t < 10T$ normalized energies of gamma photons and escaping electrons are relatively low $\varepsilon_{r,\gamma} < \varepsilon_r \lesssim \max[|E|^{max}(t < 10T)]/a_E \approx 0.28$ (equivalently, energies without the normalization are $\varepsilon_\gamma < \varepsilon \lesssim 125$ MeV). So, almost all registered photons and a major portion of the registered electrons (especially with energies $\varepsilon \gtrsim 125$ MeV, $\varepsilon_r \gtrsim 0.28$) characterize particle motion in the given field [see Figs. 7(c) and 7(d)].

As expected from Figs. 3(c) and 3(d) in the petawatt power range electrons escape mainly along the z axis [see
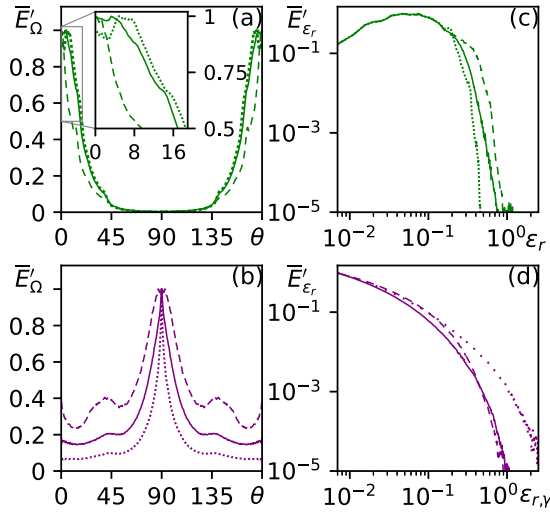
FIG. 7. (a), (b) Angular distribution and (c), (d) *relative spectrum* of escaping (a), (c) electrons and (b), (d) gamma photons as a result of irradiation of cylindrical target with radius 0.25λ and density $10n_{\mathrm{cr}}$ by the pulsed m-dipole wave with peak power 3 PW and FWHM pulse duration of 30 fs. Solid lines correspond to the simulation when photon recoil is taken into account within the quantum approach; dotted lines are obtained when the radiation reaction force in the Landau-Lifshitz form is employed; dashed lines demonstrate results without radiative effects.

Fig. 7(a)]. Radiation losses lead to approximately twice the angular spread for particles. Additionally, specific features of the classical LL radiation losses appear: dips of the angular electron distribution around $\theta = 0°$, $180°$ and an $8°$ shift of the maxima's location from these values [an insert in Fig. 7(a)]. Such shifts and dips confirm an overestimation of radiation losses in the LL case because they are observed in Figs. 3(c) and 3(d) in the quantum case not at $P = 3$ PW but at greater powers.

As in the model problem statement [see Figs. 5(a) and 5(b)], photons escape the focal region mainly in the transverse directions [see Fig. 7(b)]. Radiation losses make the photon angular distribution two times narrower in the quantum case and five times narrower in the classical LL case. Moreover, there are differences in the shape of $\overline{E}'_{\Omega}$: radiation losses lead to a convex shape at $50° < \theta < 90°$ and $90° < \theta < 130°$ with the maximum at $\theta = 90°$, while without photon recoil two additional maxima appear within a $3°$ vicinity of $\theta = 90°$.

Energy distributions of gamma photons and escaping electrons also depend on radiation losses [see Figs. 7(c) and 7(d)]. For electrons the most clear differences are at energies $\varepsilon_r \gtrsim 0.28$ [see Fig. 7(c)]. As stated above this energy range corresponds to the stage of particle motion in the given field. The NRT regime emerging at $P > P_1 = 1$ PW favors particle cooling. Also escaping electrons lose their energy in acts of photon emission in the regions of strong magnetic field even without being trapping in the NRT regime. So, in the quantum case the high energy part of *relative spectrum* is shifted to lower energies. In the classical LL case the shift is more prominent due to the overestimation of radiation losses. For photons the changes are opposite, because they originate in

the focal region, where *radial* ART emerges if photon recoil is taken into account. Particles in this regime of motion are attracted to the strongest electric field. As a result, the number of photons with the greatest energies increases [see Fig. 7(d)]. Since in the classical LL case *radial* ART is more prominent due to the overestimation of radiation losses and there is no strict limit on photon energy with regard to the energy of the parent particle, the increase of the high-energy part of *relative spectrum* is much larger than in the quantum case.

Thus, we show that with petawatt lasers there is a possibility to experimentally detect signatures of quantum radiative effects based on angular and energy spectra of particles and photons. However, it should be noted that in experiments with higher powers observation of radiative effects in particle dynamics can be obstructed by gamma photon decay into electron-positron pairs, which can strongly redistribute particles within the focus. As a result, the spectra of particles (and photons) are substantially different when pair creation is abundant. This can happen at laser powers of about 10 PW and up [63].

V. CONCLUSION

We have considered particle motion in the standing m-dipole wave in a wide range of powers from 0.01 to 300 PW and showed that the motion is distinguished by a number of unique properties. First, particle motion in the m-mode fields is not planar as in the case of the e-dipole wave. Second, particles experience a centrifugal force due to the azimuthal component of the electric field, and this force plays an important role in particle trapping effects. Third, *ponderomotive trapping*, which is distinctive for the m-dipole wave in the central region, impedes escape of particles from this region, providing the opportunity for them to accumulate influence of radiative effects and reducing the threshold of the radiation-dominated regime.

In order to determine possible modes of particle motion qualitatively and quantitatively, we have proposed averaged characteristics based on the time evolution of a particle ensemble, its spatial distribution, as well as energy and angular spectra. Based on these characteristics we have determined that even at subpetawatt powers radiative effects become noticeable owing to *ponderomotive trapping* in the region of the strongest field. At such powers radiation losses lead to *radial anomalous radiative trapping* when in the radial direction particles are attracted to the electric field antinode and in the axial direction they drift outwards from the focus. At powers greater than 1 PW *normal radiative trapping* emerges, leading to trapping and cooling of accelerated particles in the vicinity of the second electric field node. If power exceeds 25 PW, *axial anomalous radiative trapping* becomes possible between the first electric field antinode and its second node. Since field structures are asymmetric with respect to the electric field antinode, the properties of motion in *axial* and *radial* ART regimes is different. In the *axial* ART regime the motion is limited in the radial direction and is characterized by axial attraction to the focus. This is a unique regime in highly inhomogeneous fields that could result in formation of an attractor if it were not for randomness of photon emission. Nevertheless, *trapping time* is quite a steep function of power,

so remarkable long-term trapping is possible at powers above 25 PW.

We have shown that particles escape the focus mainly in the axial direction, however, ART regimes suppress axial escape and enhance transverse escape, especially at $P \gtrsim 100$ PW. In contrast, NRT favors axial escape and causes near saturation of the average energy of escaping particles at the level of 100 MeV at powers above 1 PW. We have also determined that particles emit gamma photons mainly perpendicularly to the symmetry axis and radiation losses narrow the photon distribution over the polar angle from $30°$ at 0.1 PW to $1°$ at 300 PW. The energy distribution of photons is more sensitive to regimes of particle motion than the angular distribution of photons. At subpetawatt powers *radial* ART increases the average photon energy, while the ratio of the maximal photon energy to the maximal particle energy is not influenced by radiation losses and increases with power up to about 0.8. In the power range above 1 PW NRT becomes dominant and decreases this ratio to about 0.4 at 25 PW. At greater powers *axial* ART increases this ratio, which reaches about 0.7 at above 100 PW.

Based on the obtained results we have proposed a schematic of a laboratory experiment on irradiation of a nanowire by a converging m-dipole wave. A total power of about 1 PW and pulse duration of 30 fs has been predicted to be sufficient in order to detect signatures of radiative effects.

APPENDIX A

In order to retrieve from simulations the averaged radial distribution of particles, the following procedure is carried out. First, since simulations are performed in Cartesian coordinates and the configurations of fields and particles feature axial symmetry, without loss of generality an on-axis particle distribution at $x > 0$ is considered. Second, the total number of particles in the vicinity of the x axis in ranges $z \in [-\triangle_z, \triangle_z]$ and $y \in [-\triangle_y, \triangle_y]$ is calculated as a function of time $N(t) = \int_{x=0}^{\lambda} \int_{z=-\triangle_z}^{\triangle_z} \int_{y=-\triangle_y}^{\triangle_y} n(x,y,z,t)\, d^3r$, where $n(x,y,z,t)$ is the particle density. Third, the averaged particle density along the x axis is retrieved: $n_{av}(x) = \frac{1}{sT} \int_{t=t^*}^{t^*+sT} \int_{z=-\triangle_z}^{\triangle_z} \int_{y=-\triangle_y}^{\triangle_y} \frac{n(x,y,z,t)}{N(t)}\, dt\, dz\, dy$, where s is an integer number and t^* corresponds to a moment of time when regimes of motion are steady state. The employed integration over time is needed due to radial oscillations of particles in time. The normalization is necessary because the number of particles in the focus decreases in time (see Fig. 2), and otherwise only initial moments of time may contribute to the spatial distribution significantly. Finally, we obtain the characteris-

tic spatial particle distribution as $\bar{n}(x) = n_{av}(x)/n_{av}^{\max}(x)$. In order to decrease computational noises without introducing artificial effects, the following parameters were chosen: $s = 2$; $\triangle_z = 0.1\lambda$; $\triangle_y = 0.04\lambda$. The distribution $\bar{n}(x)$ depends on t^*; however, at $t^* > t_{q=7}(P)$ [see Sec. III C for the definition of $t_q(P)$] the characteristic distribution is stabilized. We use $t^*(P) = t_{10}(P)$ in our analysis.

At the spatial resolution used in simulations (see Sec. III B) the obtained $\bar{n}(x)$ quite accurately represents $\bar{n}(\rho)$ (averaged radial distribution of particles) at any azimuthal angle due to axial symmetry. Stacking of $\bar{n}(\rho)$ obtained at different powers [examples of $\bar{n}(\rho)$ in Fig. 3(b)] gives the two-dimensional map of the averaged particle distribution $\bar{n}(\rho, P)$ presented in Fig. 3(a).

The procedure of retrieving averaged angular and energy distribution handles particles at a distance from the focal region. Let $I'_\Omega \equiv dI/d\Omega$ denote the energy dI of particles passing through the observation sphere per unit time with momentum directed into an element of solid angle $d\Omega$ in the momentum space. In our simulations the radius of the observation sphere is equal to half of the minimal size of the simulation box, namely, 3λ. The normalizing factor is equal to $I_{\Omega,n} = \int I'_\Omega\, d\Omega$. The energy of particles per solid angle averaged over time period sT is $W'_\Omega = 1/(sT) \int_{t=t^*+t_d}^{t^*+t_d+sT} I'_\Omega(t)/I_{\Omega,n}(t)\, dt$. The time delay $t_d \approx 3T$ is determined by the propagation of particles from the focal region to the observation sphere (see Sec. III D). Finally, the averaged angular characteristic of particles is $\overline{W}'_\Omega = W'_\Omega/W'^{\max}_\Omega$. Suitable parameters corresponding to stabilized angular distributions are the same as those for the spatial distribution: $s = 2$; $t^* = t_{10}$. Following $\overline{W}'_\Omega$ the averaged *relative spectrum* $\overline{W}'_{\varepsilon_r}$ can be introduced by replacing Ω with ε_r in the procedure described above with the same parameters: $s = 2$; $t^* = t_{10}$. Maps of these distributions depending on wave power are shown in Figs. 3(c)–3(f).

APPENDIX B

Due to the centrifugal force there is a certain boundary, outside which particles can be pushed out of the central region. In order to estimate the radius of this boundary near the central plane, let us suppose that at a certain radius the centrifugal force cannot be balanced by the Lorentz force. Then from Eq. (4) one may obtain that the boundary of the balance is determined by

$$m\omega B_z = p_\varphi/\rho, \tag{B1}$$

where the field is dimensionless. Since the maximal displacements of a particle from the z axis during the wave period mainly occur when the magnetic field is close to its maximal value, the instantaneous field can be replaced by its local amplitude. At this moment the azimuthal electric field is changing its direction, the vector potential is maximal and according to Eq. (6) $|p_\varphi| = |eA_\varphi/c| = mcE_m$, where E_m is the local dimensionless electric field amplitude. Using Eq. (3) we arrive at the expression for the boundary radius in the vicinity of the central plane ($z \approx 0$):

$$\rho_b = \sqrt{2.5\lambda}/2\pi \approx 0.25\lambda. \tag{B2}$$

APPENDIX C

Since the time of particle escape from the focal region is mainly determined by *trapping time* in the *axial* ART regime at $P \gg P_4 = 25$ PW, below we derive a fitting for $t_{10}(P)$ based on the properties of particle motion in this regime and the probability of photon emission.

In order to remain trapped in the *axial* ART regime after acceleration by the electric field, a particle needs to lose a significant part of its energy each half of the wave period. By analogy with the probability of photon emission by a particle [64] let us consider the probability of a particle losing a significant part of its energy during $T/2$ and consequently maintaining the trapped state as $\mathrm{Pr} = 1 - \exp\left(-\int_0^{T/2} \Psi \, dt\right)$, where Ψ denotes the probability of losing a significant part of particle energy per unit time. During $N_{0.5}$ (an integer number) halves of wave periods the probability of trapping is $\mathrm{Pr}^{N_{0.5}}$. Since t_{10} is determined as the moment when the number of particles in the focus becomes an order of magnitude less than the initial number, the corresponding number of half periods is determined by the equation

$$\mathrm{Pr}^{N_{0.5}} = 0.1, \qquad (C1)$$

and the escape time can be estimated as

$$t_{10} = 0.5 N_{0.5} T. \qquad (C2)$$

From Eq. (C1) it follows that $N_{0.5} = \ln(0.1)/\ln[1 - \exp(-\int_0^{T/2} \Psi \, dt)]$. Substituting this expression into Eq. (C2) we arrive at an estimate $t_{10} \approx 0.5 \ln(0.1) T / \ln[1 - \exp(-\int_0^{T/2} \Psi \, dt)]$. To derive rigorously the time of escape we need to compute $\int_0^{T/2} \Psi dt$ along particle trajectories. To avoid it we may assume $\int_0^{T/2} \Psi \, dt \approx a_1 P_{\mathrm{PW}}^{a_2}$ and fit numerical data, since for different field structures (as found in Refs. [13,31,32,65]) a similar integral can be approximated by a power law function of wave amplitude. The best fitting of $t_{10}(P)$ (obtained numerically in the power region $P > 25$ PW where *axial* ART manifests itself) yields $a_1 \approx 0.18$ and $a_2 \approx 0.49$, so a good approximation is

$$\bar{t}_{10}(P > 25 \text{ PW}) = \frac{0.5 \ln(0.1) T}{\ln\left[1 - \exp\left(-0.18 P_{\mathrm{PW}}^{0.49}\right)\right]}$$

$$\approx \frac{-1.15 T}{\ln\left[1 - \exp\left(-2.6 \times 10^{-4} a^{0.98}\right)\right]}. \qquad (C3)$$

[1] C. N. Danson, C. Haefner, J. Bromage, T. Butcher, J.-C. F. Chanteloup, E. A. Chowdhury, A. Galvanauskas, L. A. Gizzi, J. Hein, D. I. Hillier *et al.*, High Pow Laser Sci. Eng. **7**, e54 (2019).

[2] M. Marklund and P. K. Shukla, Rev. Mod. Phys. **78**, 591 (2006).

[3] A. Di Piazza, C. Müller, K. Z. Hatsagortsyan, and C. H. Keitel, Rev. Mod. Phys. **84**, 1177 (2012).

[4] P. Chen, Eur. Phys. J.: Spec. Top. **223**, 1121 (2014).

[5] E. Liang, T. Clarke, A. Henderson, W. Fu, W. Lo, D. Taylor, P. Chaguine, S. Zhou, Y. Hua, X. Cen *et al.*, Sci. Rep. **5**, 13968 (2015).

[6] H. Takabe and Y. Kuramitsu, High Power Laser Sci. Eng. **9**, e49 (2021).

[7] N. B. Narozhny, S. S. Bulanov, V. D. Mur, and V. S. Popov, JETP Lett. **80**, 382 (2004).

[8] A. M. Fedotov, Laser Phys. **19**, 214 (2009).

[9] S. S. Bulanov, V. D. Mur, N. B. Narozhny, J. Nees, and V. S. Popov, Phys. Rev. Lett. **104**, 220404 (2010).

[10] S. S. Bulanov, T. Z. Esirkepov, A. G. R. Thomas, J. K. Koga, and S. V. Bulanov, Phys. Rev. Lett. **105**, 220407 (2010).

[11] A. Gonoskov, I. Gonoskov, C. Harvey, A. Ilderton, A. Kim, M. Marklund, G. Mourou, and A. Sergeev, Phys. Rev. Lett. **111**, 060404 (2013).

[12] A. R. Bell and J. G. Kirk, Phys. Rev. Lett. **101**, 200403 (2008).

[13] A. M. Fedotov, N. B. Narozhny, G. Mourou, and G. Korn, Phys. Rev. Lett. **105**, 080402 (2010).

[14] E. N. Nerush, I. Y. Kostyukov, A. M. Fedotov, N. B. Narozhny, N. V. Elkina, and H. Ruhl, Phys. Rev. Lett. **106**, 035001 (2011).

[15] A. V. Bashinov and A. V. Kim, Phys. Plasmas **20**, 113111 (2013).

[16] E. G. Gelfer, A. A. Mironov, A. M. Fedotov, V. F. Bashmakov, E. N. Nerush, I. Y. Kostyukov, and N. B. Narozhny, Phys. Rev. A **92**, 022113 (2015).

[17] W. Luo, Y.-B. Zhu, H.-B. Zhuo, Y.-Y. Ma, Y.-M. Song, Z.-C. Zhu, X.-D. Wang, X.-H. Li, I. C. E. Turcu, and M. Chen, Phys. Plasmas **22**, 063112 (2015).

[18] M. Jirka, O. Klimo, M. Vranic, S. Weber, and G. Korn, Sci. Rep. **7**, 15302 (2017).

[19] M. Vranic, T. Grismayer, R. A. Fonseca, and L. O. Silva, Plasma Phys. Control. Fusion **59**, 014040 (2017).

[20] M. Tamburini, A. Di Piazza, and C. H. Keitel, Sci. Rep. **7**, 5694 (2017).

[21] Z. Gong, R. H. Hu, Y. R. Shou, B. Qiao, C. E. Chen, X. T. He, S. S. Bulanov, T. Z. Esirkepov, S. V. Bulanov, and X. Q. Yan, Phys. Rev. E **95**, 013210 (2017).

[22] A. Gonoskov, A. Bashinov, S. Bastrakov, E. Efimenko, A. Ilderton, A. Kim, M. Marklund, I. Meyerov, A. Muraviev, and A. Sergeev, Phys. Rev. X **7**, 041003 (2017).

[23] I. Gonoskov, A. Aiello, S. Heugel, and G. Leuchs, Phys. Rev. A **86**, 053836 (2012).

[24] E. S. Efimenko, A. V. Bashinov, S. I. Bastrakov, A. A. Gonoskov, A. A. Muraviev, I. B. Meyerov, A. V. Kim, and A. M. Sergeev, Sci. Rep. **8**, 2329 (2018).

[25] E. S. Efimenko, A. V. Bashinov, A. A. Gonoskov, S. I. Bastrakov, A. A. Muraviev, I. B. Meyerov, A. V. Kim, and A. M. Sergeev, Phys. Rev. E **99**, 031201(R) (2019).

[26] L. D. Landau and E. M. Lifshitz, *The Classical Theory of Fields* (Elsevier, Oxford, 1975).

[27] X.-L. Zhu, T.-P. Yu, Z.-M. Sheng, Y. Yin, I. C. E. Turcu, and A. Pukhov, Nat. Commun. **7**, 13686 (2016).

[28] T. Yuan, J. Y. Yu, W. Y. Liu, S. M. Weng, X. H. Yuan, W. Luo, M. Chen, Z. M. Sheng, and J. Zhang, Plasma Phys. Control. Fusion **60**, 065003 (2018).

[29] C. P. Ridgers, C. S. Brady, R. Duclous, J. G. Kirk, K. Bennett, T. D. Arber, A. P. L. Robinson, and A. R. Bell, Phys. Rev. Lett. **108**, 165006 (2012).

[30] Z. Lécz and A. Andreev, Plasma Phys. Control. Fusion **61**, 045005 (2019).

[31] A. A. Mironov, E. G. Gelfer, and A. M. Fedotov, Phys. Rev. A **104**, 012221 (2021).

[32] V. F. Bashmakov, E. N. Nerush, I. Y. Kostyukov, A. M. Fedotov, and N. B. Narozhny, Phys. Plasmas **21**, 013105 (2014).

[33] A. Gonoskov, A. Bashinov, I. Gonoskov, C. Harvey, A. Ilderton, A. Kim, M. Marklund, G. Mourou, and A. Sergeev, Phys. Rev. Lett. **113**, 014801 (2014).

[34] A. I. Nikishov and V. I. Ritus, Zh. Eksp. Teor. Fiz. **46**, 776 (1964) [Sov. Phys. JETP **19**, 529 (1964)].

[35] I. V. Sokolov, N. M. Naumova, J. A. Nees, and G. A. Mourou, Phys. Rev. Lett. **105**, 195005 (2010).

[36] A. A. Mironov, N. B. Narozhny, and A. M. Fedotov, Phys. Lett. A **378**, 3254 (2014).

[37] A. S. Samsonov, E. N. Nerush, and I. Y. Kostyukov, Sci. Rep. **9**, 11133 (2019).

[38] I. I. Artemenko and I. Y. Kostyukov, Phys. Rev. A **96**, 032106 (2017).

[39] A. M. Fedotov and A. A. Mironov, Phys. Rev. A **88**, 062110 (2013).

[40] C. Slade-Lowther, D. Del Sorbo, and C. P. Ridgers, New J. Phys. **21**, 013028 (2019).

[41] A. M. Fedotov, N. V. Elkina, E. G. Gelfer, N. B. Narozhny, and H. Ruhl, Phys. Rev. A **90**, 053847 (2014).

[42] J. G. Kirk, Plasma Phys. Control. Fusion **58**, 085005 (2016).

[43] A. V. Bashinov, A. A. Gonoskov, A. V. Kim, M. Marklund, G. Mourou, and A. M. Sergeev, Quantum Electron. **43**, 291 (2013).

[44] I. A. Surmin, S. I. Bastrakov, E. S. Efimenko, A. A. Gonoskov, A. V. Korzhimanov, and I. B. Meyerov, Comput. Phys. Commun. **202**, 204 (2016).

[45] A. Gonoskov, S. Bastrakov, E. Efimenko, A. Ilderton, M. Marklund, I. Meyerov, A. Muraviev, A. Sergeev, I. Surmin, and E. Wallin, Phys. Rev. E **92**, 023305 (2015).

[46] V. N. Bayer, V. M. Katkov, and V. S. Fadin, *Radiation of the Relativistic Electrons* (Atomizdat, Moscow, 1973).

[47] J. M. Cole, K. T. Behm, E. Gerstmayr, T. G. Blackburn, J. C. Wood, C. D. Baird, M. J. Duff, C. Harvey, A. Ilderton, A. S. Joglekar *et al.*, Phys. Rev. X **8**, 011020 (2018).

[48] K. Poder, M. Tamburini, G. Sarri, A. Di Piazza, S. Kuschel, C. D. Baird, K. Behm, S. Bohlen, J. M. Cole, D. J. Corvan *et al.*, Phys. Rev. X **8**, 031004 (2018).

[49] A. V. Bashinov, P. Kumar, and A. V. Kim, Phys. Rev. A **95**, 042127 (2017).

[50] J. G. Kirk, A. R. Bell, and I. Arka, Plasma Phys. Control. Fusion **51**, 085008 (2009).

[51] S. V. Bulanov, T. Z. Esirkepov, J. K. Koga, S. S. Bulanov, Z. Gong, X. Q. Yan, and M. Kando, J. Plasma Phys. **83**, 905830202 (2017).

[52] A. V. Bashinov, P. Kumar, and A. V. Kim, Quantum Electron. **48**, 833 (2018).

[53] A. V. Bashinov, P. Kumar, and E. S. Efimenko, Quantum Electron. **49**, 314 (2019).

[54] A. Savitzky and M. J. E. Golay, Anal. Chem. **36**, 1627 (1964).

[55] G. Lehmann and K. H. Spatschek, Phys. Rev. E **85**, 056412 (2012).

[56] See Supplemetal Material at http://link.aps.org/supplemental/ 10.1103/PhysRevE.105.065202 for more details of particle motion in different regimes.

[57] J. T. Mendonca and F. Doveil, J. Plasma Phys. **28**, 485 (1982).

[58] Z.-M. Sheng, K. Mima, Y. Sentoku, M. S. Jovanović, T. Taguchi, J. Zhang, and J. Meyer-ter-Vehn, Phys. Rev. Lett. **88**, 055004 (2002).

[59] A. S. Samsonov, E. N. Nerush, and I. Y. Kostyukov, Phys. Rev. A **98**, 053858 (2018).

[60] V. B. Berestetskii, E. M. Lifshits, and L. P. Pitaevskii, *Quantum Electrodynamics* (Pergamon Press, New York, 1982).

[61] T. N. Wistisen, A. Di Piazza, H. V. Knudsen, and U. I. Uggerhøj, Nat. Commun. **9**, 795 (2018).

[62] A. Taflove and S. Hagness, *Computational Electrodynamics: The Finite-Difference Time-Domain Method* (Artech House, Boston, 2005).

[63] A. V. Bashinov, E. S. Efimenko, A. A. Muraviev, V. D. Volokitin, I. B. Meyerov, G. Leuchs, A. M. Sergeev, and A. V. Kim, arXiv:2103.16488.

[64] R. Duclous, J. G. Kirk, and A. R. Bell, Plasma Phys. Control. Fusion **53**, 015009 (2011).

[65] I. Y. Kostyukov and E. N. Nerush, Phys. Plasmas **23**, 093119 (2016).